Available online at www.eccomasproceedia.org
Eccomas Proceedia UNCECOMP (2019) 1-19

ECCOMAS
Proceedia

UNCECOMP 2019
3rd ECCOMAS Thematic Conference on
Uncertainty Quantification in Computational Sciences and Engineering
M. Papadrakakis, V. Papadopoulos, G. Stefanou (eds.)
Crete, Greece, 24-26 June 2019

AGGREGATE CLUSTERING AND CASTING DIRECTION EFFECTS IN LATTICE DISCRETE PARTICLE MODEL SIMULATIONS

Jan Podroužek[1,2], Marco Marcon[1], Jan Vorel[1,3], and Roman Wan-Wendner[1,4]

[1]Christian Doppler Laboratory LiCRoFast, Department of Civil Engineering and Natural Hazards,
University of Natural Resources and Life Sciences (BOKU)
1190 Vienna, Austria
e-mail: marco.marcon@boku.ac.at

[2]Faculty of Civil Engineering, Brno University of Technology
602 00 Brno, Czech Republic
e-mail: podrouzek.j@vutbr.cz

[3]Faculty of Civil Engineering, Czech Technical University, Prague (CTU)
166 29 Praha 6, Czech Republic
e-mail: jan.vorel@fsv.cvut.cz

[4]Department of Structural Engineering, Faculty of Engineering and Architecture, Ghent University
9052 Ghent, Belgium
e-mail: roman.wanwendner@ugent.be

Abstract. *The paper aims at characterizing the influence of particle placement and clustering in lattice discrete particle model (LDPM) simulations of concrete on structural response. The presented spatial variability package for LDPM enables for the first time to influence the previously independent and random particle placement. The proposed scheme correlates the particle placement to an initial random or gradient-based fields in order to mimic some of the experimentally observed phenomena such as aggregate clustering or the effect of casting direction. The study is based on high-dimensional Monte Carlo (MC) LDPM simulations of three classical concrete tests in which the inherent variability and production process are represented by the proposed particle placement schemes with varying parameters. The material property fields are kept constant at this phase of the investigation in order to isolate and quantify the potential effect of the proposed particle placement schemes on structural response. This investigation is based on a comparison of stress and strain values at peak for different tests against the case of independent and random placement. The coefficients of variation of the above-mentioned outputs are also evaluated. This research aims at evaluating the importance influencing the particle placement according to experimentally measurable phenomena before initiating research on the spatial variability of material properties and the respective correlation structure.*

Keywords: Spatial Variability, Concrete, Autocorrelation length, Concrete Failure, Monte Carlo

ISSN:2623-3339
Peer-review under responsibility of the organizing committee of UNCECOMP 2019.
doi: 10.7712/120219.6321.18788

1 Introduction

According to classical theories and some already outdated codes [1, 2] the nominal strength of geometrically similar structures made from non-random materials is independent of the structural size. The application of random heterogeneous media, however, such as concrete, require higher order theories [3] for a safe and economical design, especially when large or slender structures are considered. The scattering of physical experiments [4] and occasional structural failures [5], however, do not always comply with such theories, even if current probabilistic approaches are introduced. While the energetic size effect is relevant regardless if the material is heterogeneous or not there is also a statistical size effect linked to the spatial variability of heterogenous materials.

In Monte Carlo (MC) based probabilistic simulations [6], the random material properties are typically considered spatially uniform and as such are assigned to structural members or entire structures. This simplification is important for the formulation of MC sampling schemes [6, 7], required for feasible tail characterization of structural response (engineering failure probabilities).

On the other hand, neglecting the spatial variability means that the most fundamental concepts in structural reliability cannot be directly captured by simulations. Clearly, if random fields are introduced to MC based probabilistic simulations, the established sampling schemes cannot be applied, and the outcome of applying random fields is limited to answering what-if scenarios. The reason can be found in the extreme dimensionality of the problem combined with unknown sensitivity.

Recent developments in sampling schemes for spatial or temporal variability are discussed by [7, 8, 4], where a feasible sample selection strategy for spatial variability is proposed. With the introduction of random (spatially variable) fields in the MC simulations the question of autocorrelation quickly emerges as the amount of response scattering, e.g. in terms of COV (coefficient of variation) of load capacity, becomes sensitive to particular parameters of the random field. These are most typically the functional form of the autocorrelation function and its coefficients, which can be linked to a characteristic length, both mimicking the micro-structural features of a particular (composite) material and production processes [9, 10, 11, 12]. The introduction of spatial variability to discrete meso-scale simulations of concrete has been previously done by [13], who experimented with randomized material property fields and thin, nearly 2D, specimens.

This paper is unique in directly linking the micro-structural features of the random heterogeneous material to the COV of response by the investigated particle placement schemes, which are governed by the initial spatial field, while maintaining the material property fields constant. Moreover, the investigated classical concrete specimens are investigated fully in 3D, which results in a number of qualitatively different failure modes and crack paths, aside from the ability to capture the relationship between the COV of response and the particular correlation structure. In particular, gradient-based fields and random fields are introduced into the stochastic framework of the lattice discrete particle model (LDPM) to account for the inherent variability and production processes of several concrete specimen test series (Figure 4), such as cylinder and cube compression tests, and unnotched three point bending tests. As a consequence, the lattice models become sensitive to a particular particle placement concept, which is no longer independent and random [4], and the scattering of the response can, thus, be controlled and associated with the physical meaning of an auto-correlation length (6 values tested) and particular form of the spectral function (1 value tested in this paper). The aim of this contribution is

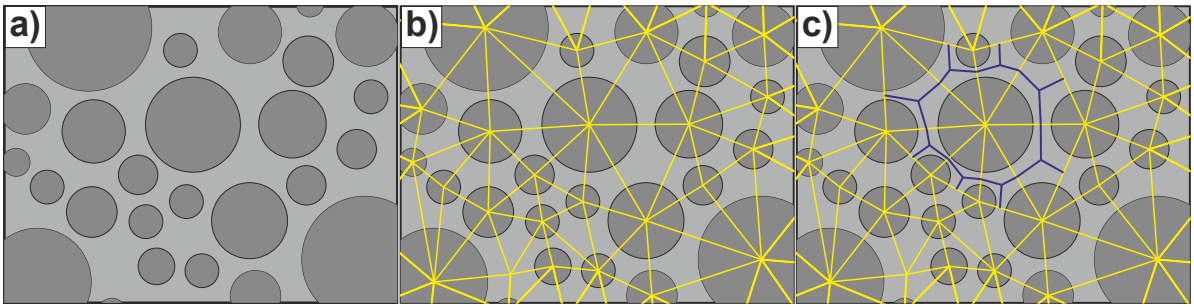

Figure 1: 2D representation of the LDPM polyhedral cell construction. a) Particle placement, b) Lattice mesh and tetrahedralisation, and c) Domain tessellation.

to evaluate the influence of such particle placement schemes on the structural response having constant material property fields. Only in a second step also the spatial variability in material properties and the respective correlation structure will be investigated. Due to complex nature of the investigated problem it is essential to first isolate and quantify the importance of mimicking clustering and directional effects by the later proposed particle placement schemes.

2 Lattice Discrete Particle Model (LDPM)

A well-established member of the discrete framework, the lattice discrete particle model (LDPM), has been extensively calibrated and validated. It has shown superior capabilities in reproducing and predicting concrete behaviour [14, 15, 16, 17, 18] in a number of practically relevant applications. It simulates the meso-structure of concrete by a three-dimensional (3D) assemblage of particles that are generated randomly according to a given grain size distribution. Figure 1 shows a 2D representation of the LDPM polyhedral cell construction. After the particles are randomly placed in the concrete domain from the biggest to the smallest (Figure 1a), the lattice mesh is generated connecting the centers of the spheres (Figure 1b). Delaunay tetrahedralization and 3D domain tessellation (Figure 1c) are used to generate the system of cells interacting through triangular facets (blue lines in the 2D representation). Note that even though spherical aggregates are assumed for the purpose of generating the particle distribution the final discretization consists of polyhedral cells as sketched in Figure 1c) for the 2D case.

Displacements and rotations of such adjacent particles form the discrete compatibility equations in terms of rigid body kinematics. At each cell facet the meso-scale constitutive law is formulated such that it simulates cohesive fracture, compaction due to pore collapse, frictional slip and rate effect. For each single particle equilibrium equations are finally formulated. An extended version of LDPM is currently developed and simulates various deterioration mechanisms, such as e.g. the Alkali-Silica reaction (ASR) [16], creep and shrinkage. Creep analyses are performed in a rate type form based on code models [19] or by utilizing the Micro-Prestress Solidification Theory MPS [20, 21, 22, 23, 24]. A further development is the age-dependent LDPM framework in which the local material properties are derived by chemo-mechanical coupling from a chemo-hygro-thermal model [25, 26].

3 Characterization of internal structure

If studied at a particular scale and quantity, random heterogeneous materials, such as concrete, exhibit clustering features, which cannot be mimicked by the current LDPM version, where particles are placed randomly and independently. Literature offers a number of approaches on how to describe, quantify, reproduce and compare observed and artificially gen-

erated spatially variable structures (spatial arrangement and heterogeneity of micro-structural features). Since the scope of this paper does not allow to cover all classes of statistical descriptors, please refer e.g. to [27, 28, 29] for review. Among the classical approaches allowing for the inference of correlation length (or in general the length scale parameters that characterize spatial heterogeneity and clustering) is the two-point, three-point, and higher order microstructural correlation functions [30], the Ripley's functions and its derivatives [31], the Lineal-Path Function, Chord-Length Density Function, Pore-Size Functions, or the Two-Point Cluster Function [29]. The increasingly available computing resources enabled the practical utilization of morphological-based analyses, which may be more suitable for smaller domain to feature size ratios, i.e. instances where the system size is not sufficiently larger that the correlation length of interest.

The authors briefly introduce here an original approach, which is both computationally efficient and robust, and is based on the Mean value of Minimum Euclidean Distance between centres of fitted circles (MMED). This approach requires that the originally continuous random field is binarized. By using standard image processing, object recognition and morphological analysis algorithms, the boundary components and possibly small components are deleted and subsequently the circular objects (circles) are detected (see Figure 3). Then, for each circle center coordinate a nearest (in euclidean space) neighbour is identified and the correlation length then corresponds to the mean value of such (nearest neighbour) distances. The detection and measurements of objects is based on a local feature detector and descriptor SURF algorithm [32], where the circular objects can be replaced by fitted ellipses or any other parametric shapes. The binarization process is governed by the Otsus cluster variance maximization method [33]. Please note that the correlation lengths in this paper are understood as relative measure, since the random field realizations are self-similar at various scales and independent on the resolution. In fact, this corresponds to various power spectral function parameter sets.

This way, it is ensured that although each specimen has different physical and discretization size, the same patters for the same power spectral function parameters emerge relative to the size of the specimen. The absolute values of the correlation length can be obtained by simply multiplying the relative value of the correlation length with the maximum size of the bounding box of the specimen, d. This is due to the fact that the random fields are initially generated in a $d \times d \times d$ box lattice.

A large number of paradigms related to the generation of correlated spatially variable structures (random fields) exists, including classical algebraic approaches, such as e.g. Fourier transformation [34], Karhunen-Love approximation [35], Polynomial chaos decomposition [36], or evolutionary algorithms, such as cellular automata [37], offering various levels of control in the achieved correlation, variance or stationariness, to name a few. Various production artefacts, such as casting process, can also be simulated by the classical or mesh-less particle-based computational fluid dynamics, possibly also coupled with discrete element method (DEM) [38]. The material structure can be also There is still an ongoing debate concerning the optimal model, mostly from a mathematical and philosophical perspective, since very little is yet known at the required (statistically relevant) level on structural materials.

Given the dimensionality of the problem and the aformentioned arguments, a simple model for the generation of random field has been adopted. It is based on a discrete inverse Fourier transform of a product of noise and amplitude. The noise is defined as a discrete Fourier transform of a pseudo-random variate from a symbolic (Gaussian) distribution and the amplitude is defined by an arbitrarily chosen spectral (autocorrelation) function [34].

In the literature, several functional forms are proposed for autocorrelation functions (Fig-

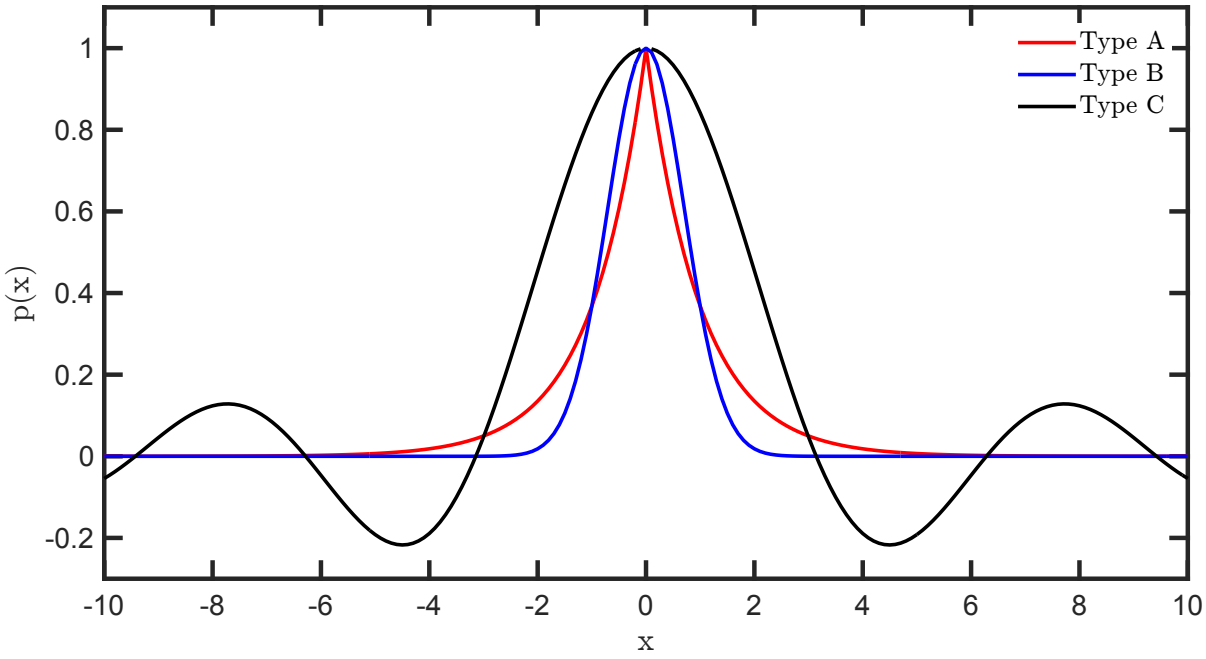

Figure 2: Comparison of the structurally relevant autocorrelation functions from the literature, scale of fluctuation equals to 2.

Table 1: Power spectral function exponents ($pfse$) and related relative autocorrelation length (RAL). The RAL is relative to the maximum specimen size.

a	3.5	3.0	2.5	2.0	1.5	1.0
RAL	18.36 %	7.81 %	4.69 %	3.52 %	3.13 %	2.73 %

ure 2). However, the proposed estimates for their coefficients vary in the order of magnitudes [39, 11, 40, 41] due to their different (physical) interpretation and due to the fact that random heterogeneous materials in general can be considered fractal, i.e. statistically self-similar on a range of length scales. Also, often different equations or names can be found describing the same functional form. Therefore, similarly to the question of generating random fields, the simplest form has been assumed, which corresponds to Type A from Figure 2 which presents the spectral functions $p(x)$ for continuous distance, x. Note that by definition, the spectral density function must be non-negative. The investigated power spectral function with exponent a reads:

$$p(x) = 1/(x^a) \tag{1}$$

The herein adopted meaning of autocorrelation length should follow from Figure 3a (MMED applied to periodic field), while the basis for quantification of a particular autocorrelation length for random fields using the proposed MMED is depicted in Figure 3b. The particular values of relative autocorrelation lengths (RAL) compared to size d of the bounding box depend on the power spectral function exponent (coefficient a in Equation 1) and are listed in Table 1.

The absolute values of the correlation length depend on the maximum values of the bounding box of the specimens, i.e. 400, 300 and 150 mm (beam, cylinder and cube, respectively) and can be computed by simply multiplying the latter sizes by the relative correlation lengths, i.e. ranging from 73 mm for the beam with a = 3.5, to 4 mm for the cube with a = 1.0.

The proposed particle placement schemes may influence the scattering and asymptotic prop-

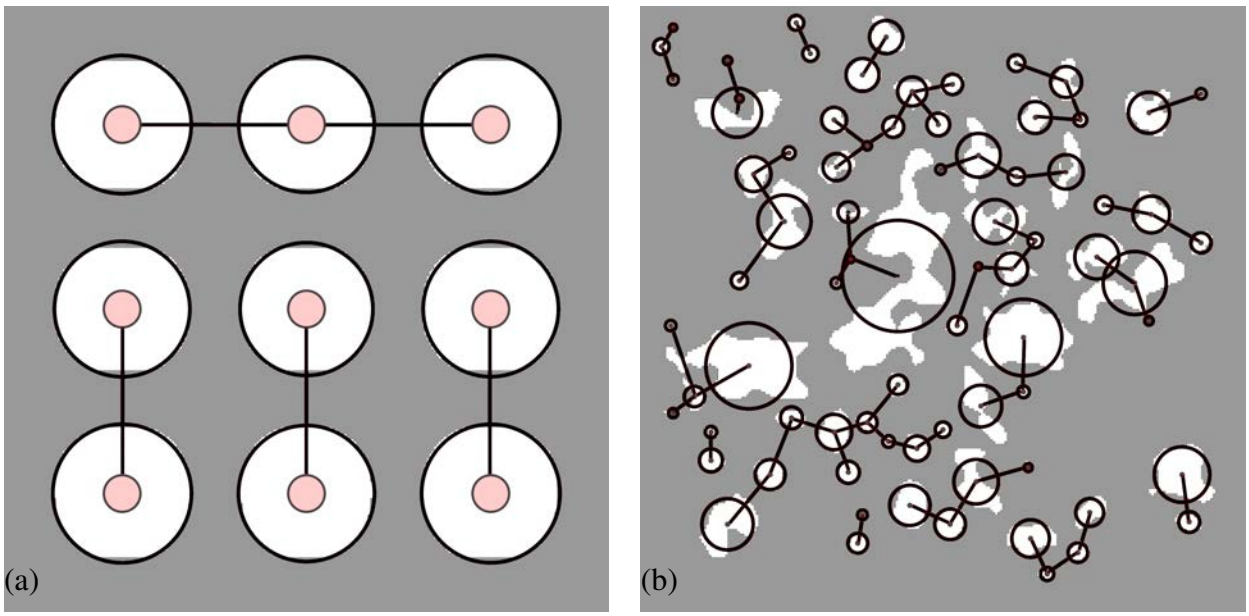

Figure 3: a) MMED applied to periodic field to illustrated the meaning of correlation length (mean distance between nearest neighbours), and b) MMED applied to binarised random field to illustrated the meaning of correlation length.

erties of the spatially variable models and, thus, contribute to the general understanding of the physics and reliability of spatial variability [42, 43]. The abstraction levels for LDPM are categorized as following [43]:

- Independent and random particle placement (IRPP);
- IRPP combined with random or gradient-based field for material characterization only;
- Particle generation governed by a field (PGGF).

Independent and random particle placement (IRPP) Independent and random particle placement and random diameter according to the size distribution curve and required volume fraction, as is currently implemented in the LDPM [14]. No conflicting requirements are to be solved. Overlapping or less than minimum distance particles are re-sampled.

IRPP combined with random or gradient-based field for material characterization only The second abstraction level assumes the original particle placement scheme, i.e. the IRPP, combined with one or more random fields, which are used to describe local fluctuations of material properties resulting from the inherent variability (random field) and construction or transport processes (gradient-based fields). Similarly to the previous case, there are no geometry-related conflicting requirements. Overlapping or less than minimum distance particles are re-sampled. Boundary regions may be normally populated by adopting a simple modification to the re-sampling algorithm.

Material characterizations derived from random fields must be verified for inadmissible values, such as negative strength, modulus, etc. This may lead to a conflict if the governing probability distribution used for generating the random field is to be maintained. Otherwise, truncated distributions may be used or the realizations of random field can be rescaled to fit the admissible range [13, 4, 44].

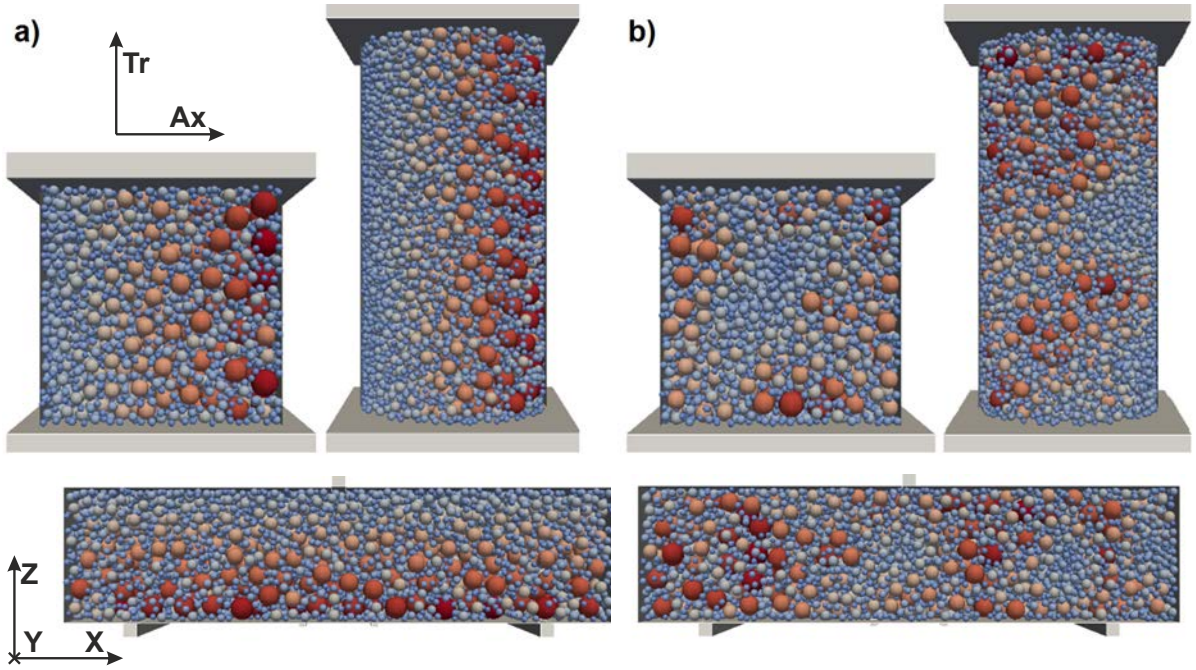

Figure 4: Visual representation of particle placement governed a) by gradient field (PGGF-G) and b) by a random field (PGGF-R).

Particle generation governed by a field (PGGF) Here it is assumed that an initial random (PGGF-R) or gradient-based (PGGF-G) field of choice (or their arbitrary combination) is governing not the material properties (optional), but the particle generation process (i.e. the position and/or the size of each particle). If the particle generation is to be governed not only by granulometric distributions, but also by a gradient-based field (PGGF-G, Figure 4a) or an initial random field (PGGF-R, Figure 4b), the particle generation becomes a complex problem and has to be approached by balancing trade-offs between conflicting goals.

Clearly, the global requirement to follow a particular size distribution can lead to a local conflict with the initial random field, the role of which can be further ambiguous if we consider it to affect both the position and size of the particles (clustering of large particles). Details regarding the associated steps/choices for random fields were published by [43, 45] and are detailed in 4.1 PGGF implementation.

For higher volume fractions this becomes a computationally expensive procedure, however local conflicts can be resolved in parallel and terminate with the first valid particle. The advantage of the approach lies in the compatibility of the mimicked meso-structure (lattice geometry) with any considered material property field (via governing random field) which otherwise cannot be maintained. This enables to verify the relationship between spatial variability, autocorrelation length of the random fields, type of spectral function and meso/micro-structure of the material which is an open research question. Ultimately, it is the goal to investigate the interaction of meso-structure and material property fields derived from the same or related random fields.

However, in a first step the statistical consequences of different particle generation schemes are investigated and compared to each other and the reference, the IRPP. For this purpose, the material properties remain spatially constant and are not derived from fields.

Table 2: LDPM mix design and main LDPM mesoscale properties. The parameters explanation can be found in [14, 15].

Mix Design LDPM parameters			**Mesoscale LDPM parameters**		
Cement content	240	kg/m^3	Elastic modulus	41000	MPa
Water/Cement	0.83	-	Poissons ratio	0.18	-
Aggregate/Cement	8.83	-	Tensile strength	2.54	MPa
Fullers coefficient	0.5	-	Softening exponent	1	-
Min. aggregate size	4	mm	Shear/Tensile strength	1.85	-
Max. aggregate size	18	mm	Tensile charact. length	200	mm

4 Numerical models

In this section, the numerical models of classical concrete experiments are introduced. Important inputs for the models are the maximum and minimum aggregate sizes. The higher bound of the sieve curve is defined by the maximum aggregate size (d_a) while the minimum aggregate size (d_0) defines its arbitrary lower cut-off, i.e. the diameter under which no particles are discretely generated and placed. Thus, the minimum aggregate size affects the refinement of the discrete mesh and consequently also the computational cost. The concrete parameters used for the LDPM in this contribution are taken from [18] since they were calibrated and validated on an experimental dataset. The main LDPM parameters along with the mix design parameters are defined in Table 2. Their explanation can be found in the original LDPM papers by Cusatis at al.[14, 15].

The simulations include cubes and cylinders loaded in compression, and unnotched beams loaded in a three point bending configuration. Cubes with an edge length of 150 mm and cylinders with a length of 300 mm and a diameter of 150 mm are considered. For both cubes and cylinders, the loading platens are modeled as rigid bodies. The unnotched beam has dimensions of $100 \times 100 \times 400$ mm and a span length between the supports of 300 mm. A visual representation of the specimens is shown in Figure 4. Figure 4a shows the three specimens' geometry having the particle placement distorted with a gradient based field while Figure 4b illustrates the particle placement according to a random field.

In the compression tests, friction between the concrete specimens and the steel platens is considered by a constraint algorithm implemented in the numerical framework MARS [46]. This algorithm constrains the surface nodes of the LDPM domain to the surface of the steel platens based on the friction coefficient $\mu(s)$, according to a contact algorithm described in a previous work by Cusatis et al. [47]. Such friction coefficient is dependent on the contact cumulative slippage s, on the static friction coefficient μ_s, on the dynamic friction coefficient μ_d, and on a characteristic length s_0 derived from fitting available test data (see [48]). The relation is described by: $\mu(s) = \mu_d + (\mu_s - \mu_d)s0/(s + s_0)$. For the cubes, aiming at simulating the contact between concrete and smooth steel, parameters $\mu_s = 0.13$, $\mu_d = 0.015$, and $s_0 = 1.3$ mm were used. For the cylinders, aiming at simulating the contact between concrete and a Teflon sheet on the steel platens, parameters $\mu_s = 0.03$, $\mu_d = 0.0084$, and $s_0 = 0.0195$ mm were used.

The loading speed for the beams was 2 mm/s, 8 mm/s for the cubes, and 5 mm/s for the cylinders. All simulations are run using a dynamic explicit solver implemented in MARS which ensures convergence at the price of computational cost due to the small stable time steps required. For all the models the kinetic energy has been monitored and limited to acceptable levels. As

already mentioned, for the PGGF-R analyses of all the geometries, the power spectral function exponent a used in the simulations was chosen to be between 1.0 and 3.5 with a discrete step of 0.5 which means having a relative autocorrelation length range between 2.7% and 18.4% of the maximum specimen dimension.

For the PGGF-G compression specimens, two directions were chosen for the gradient based field. The direction along which the top plate moves to compress the specimen is identified as Ax direction, while the direction transversal to the loading is identified as Tr. For the PGGF-G beams, their dimensions, considering the three Cartesian orthogonal directions, are: 100 mm in the Z and Y directions and 400 mm in the X direction. The load and the two supports are acting along the Z direction. In this case, one gradient field along the Y direction (Y^+) and two gradient based fields in the Z directions are analysed. The two directional fields which are along the Z directions have opposite orientation (Z^+ has the same orientation of the load, and Z^- has the opposite orientation).

Each of the simulations was run in the Vienna Scientific Cluster which consists of 2020 nodes, (8 cores with 2.6 GHz) using one node each for about 3 hours.

4.1 PGGF implementation

Particle generation governed by a field is a modified version of a standard geometrical characterization of the concrete mesostructure presented in [14].

In the present study, the generated mesostructure has to follow both the particle distribution curve and the distribution of a given (random, directional, etc.) field. In the first step, particles represented by spheres are generated following the defined concrete granulometric distribution, the interested reader is referred to [14]. The main difference between the standard and the new procedure lies in the particle placement phase during which the particle centers are placed throughout the volume of the specimen one by one (from the largest to the smallest). Assuming that N_0 particles have to be placed, N_0 random particle positions are generated and the intensity for each of them is evaluated based on the prescribed field. The positions are then ordered following the given intensity (from the highest to the lowest) and the position with the highest intensity is assigned to the largest particle. The largest particle is then placed at this position (assuming that it does not cross the border of the domain) and both the particle and the position are deleted from their lists. Next, the new position with the highest intensity is utilized to place the new largest particle (previously second in the particle list). If there is no conflict with the previously placed particle(s) and the boundary of the domain, the particle is placed and again deleted from the list. However, if it exceeds the domain boundary or overlaps with the previously placed particle(s), this position is discarded, a new random position is generated and the intensity for it is evaluated. Then the positions are again ordered based on the given intensity and the particle placing procedure continues as described before. To minimize the geometrical bias of the discretization, a minimum distance between two adjacent particles is defined as $\delta_s\,(r_1 + r_2)$, where $r_{1,2}$ stand for the radii of the particles and $\delta_s \geq 0$ is the non-dimensional scaling parameter. The utilized minimum distance rule allows a smaller distance between small and large particles compared to the distance between two large particles. $\delta_s = 0.1$ is utilized in the current study.

Specific examples and alternative choices regarding the particle placement algorithm are presented in [45].

Table 3: IRPP results of different geometries with 20 repetitions. The COV is expressed in $\%$.

Type	Property	Beam	Cylinder	Cube
IRPP	F@P (MPa,kN)	11.12±2.82%	21.50±0.41%	26.20±0.55%
	D@P (−,mm)	0.0389±4.51%	0.0012±1.18%	0.0017±3.58%

5 Results discussion

The presented observations are based on an unique and extensive computational campaign involving in total 600 simulations. Given the dimensionality of the problem, it is hard to separate physically or mechanically relevant sources of response scattering from the noise components, owing to model uncertainties (solution and discretiztion artefacts) [49].

Along with simulations in which the particle generation is governed by a field (PGGF), also the independent and random particle placement (IRPP) simulations were run for direct comparison. In all cases, 20 repetitions per specimen configuration were run. The results used in the comparison are: the mean stress or the mean force at peak (mean $F@P$) for compression specimens and beams respectively, and the mean strain or the mean displacement at peak (mean $D@P$) for compression specimens and beams respectively. Also their coefficient of variations were computed for the comparison. Table 3 shows the IRPP results for the three geometries.

Table 3 shows that, for the 20 repetitions done for the three geometries, the $COVs$ of $D@P$ are generally higher than the COV of the $F@P$. Also, it can be noticed that the compressive tests results have lower COV than the test results of the beams. This can be explained by different failure mechanism in tension and in compression. In case of flexural failure (tension) there is just one main crack that propagates and ultimately leads to failure, while in case of compression, there are many small cracks that together lead to failure. Each small crack finds its own preferential (least energy) path but in the process causes local stress redistributions affecting the other cracks so that in the end, effects average out and the response for individual realisations stay quite close to the overall mean.

The PGGF results are presented with the same nomenclature as introduced for the IRPP. Also for the PGGF simulations, 20 repetitions per configuration were run. Figure 5 shows the results for different geometries of PGGF-R with $a = 3$ (which means that the RAL is 7.8$\%$ of the maximum size of the specimen). The solid line represents the average numerical result; the numerical results' envelope is plotted as grey area. As can be seen, the 20 repetitions lead to relatively small scatter both in terms of $F@P$ and $D@P$. Note that the simulated unnotched beams experience a snap-down instability in the early post-peak, as expected in displacement control. Nevertheless, the explicit simulations up to this point fully converge with an acceptable amount of kinetic energy in the explicit simulations. Therefore, load and displacement values at peak can be considered correct and serve for this investigation.

The figure shows for the beam case, in comparison with the IRPP results, that the mean values increase while the $COVs$ decrease. For the compression specimens the mean $F@P$ decreases while its scatter increases.

All the PGGF results are shown in Figure 6. On the left Y axes of each figure, the coefficients of variation of $D@P$ and $F@P$ are plotted in red empty square markers, while the right Y axes represent the mean $D@P$ and $F@P$ in black full diamonds. The straight lines represents the IRPP related results. Figures 6(a-b) present the beams results, figures 6(c-d) the cylinders results, and figures 6(e-f) the cube results. The left figures show the PGGF-G results while the right ones show the PGGF-R results.

Regarding the directional field beam (Figure 6a), the results show very consistent trends

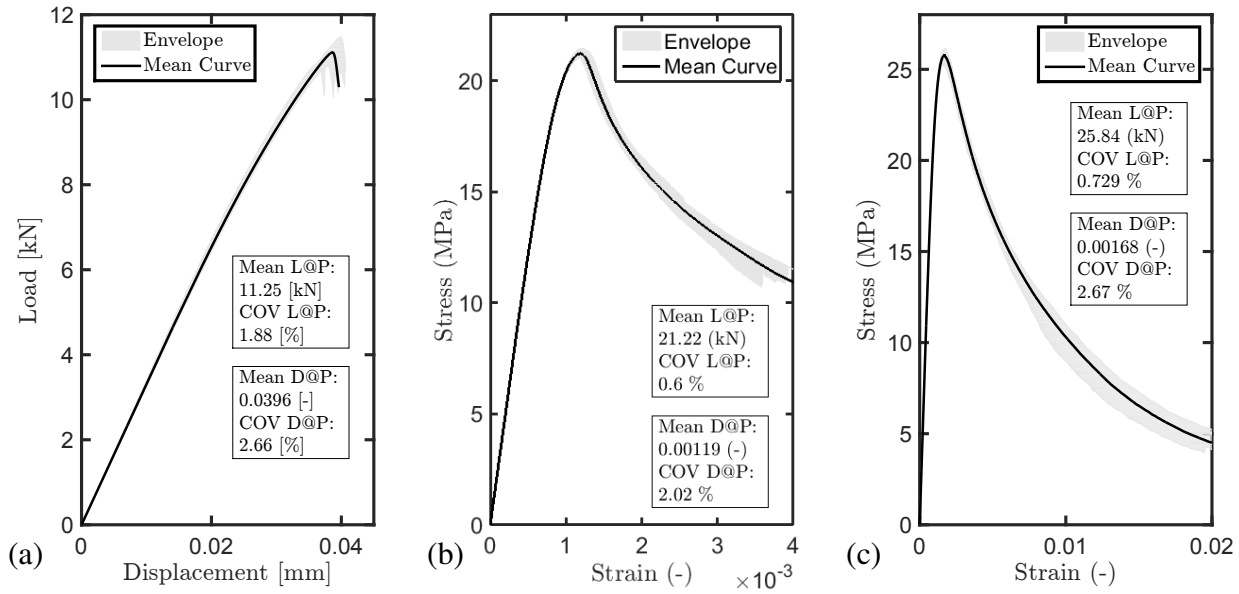

Figure 5: Results of a) Beams, b) Cylinders and c) Cubes for PGGF-R with $a = 3$

among the three different directions both in terms of mean values and in terms of COV. Regarding the random field results (Figure 6b), some weak trends can be noticed. The mean values tend to increase with the autocorrelation length, while the COV tends to stay constant. In comparison with the IRPP beam results, for the PGGF-R both the mean $F@P$ and $D@P$ increase while their $COVs$ decrease. This can be explained by the clustering of big and small particles during the particles placement. With the clustering, some weaker and stronger areas are created, causing the fracture surface to deviate from the nominal path in order to follow the least energy consuming path for its propagation.

The cylinder results are shown in Figure 6(c-d). The directional field results (Figure 6c) show noticeable differences between the axial direction and the tangential direction field. Even though it can be noticed that the transversal direction has higher mean values and COV (compared with the longitudinal one), this doesn't happen for the COV of the peak load which is smaller for the transversal direction. The PGGF-R cylinder results (Figure 6d) show stronger trends compared with the beam case. The trend of the mean $D@P$ and $F@P$ is decreasing with the autocorrelation length while, the trend of the COV is increasing with it. In comparison with the IRPP results, the $D@P$ mean and COV tend to increase; the mean $F@P$ decreases while the COV keeps similar values.

Figure 6(e-f) present the cube results. As for the cylinder, the PGGF-G show that one of the curves, (in this case the mean $D@P$) deviates from the main trend. The PGGF-G results (Figure 6f) show no clear trends for the mean values or the COV.

In comparison with the IRPP cube results, the mean values of $D@P$ and $F@P$ decrease while their COV stays approximately constant. As could be seen from this summary, for the compression geometries the mean $F@P$ tends to be smaller for the $PGGF$ field. In case of the beam only one macro-crack forms and ultimately causes failure, depending on its path across the specimen. For the compression specimens, multiple cracks lead to failure and in this case the clustering lead to a reduction of the peak load.

Please also note the purpose of this study was not to generate (increased) scatter in LDPM simulations, but to quantify scattering caused by the particle placement algorithm independent

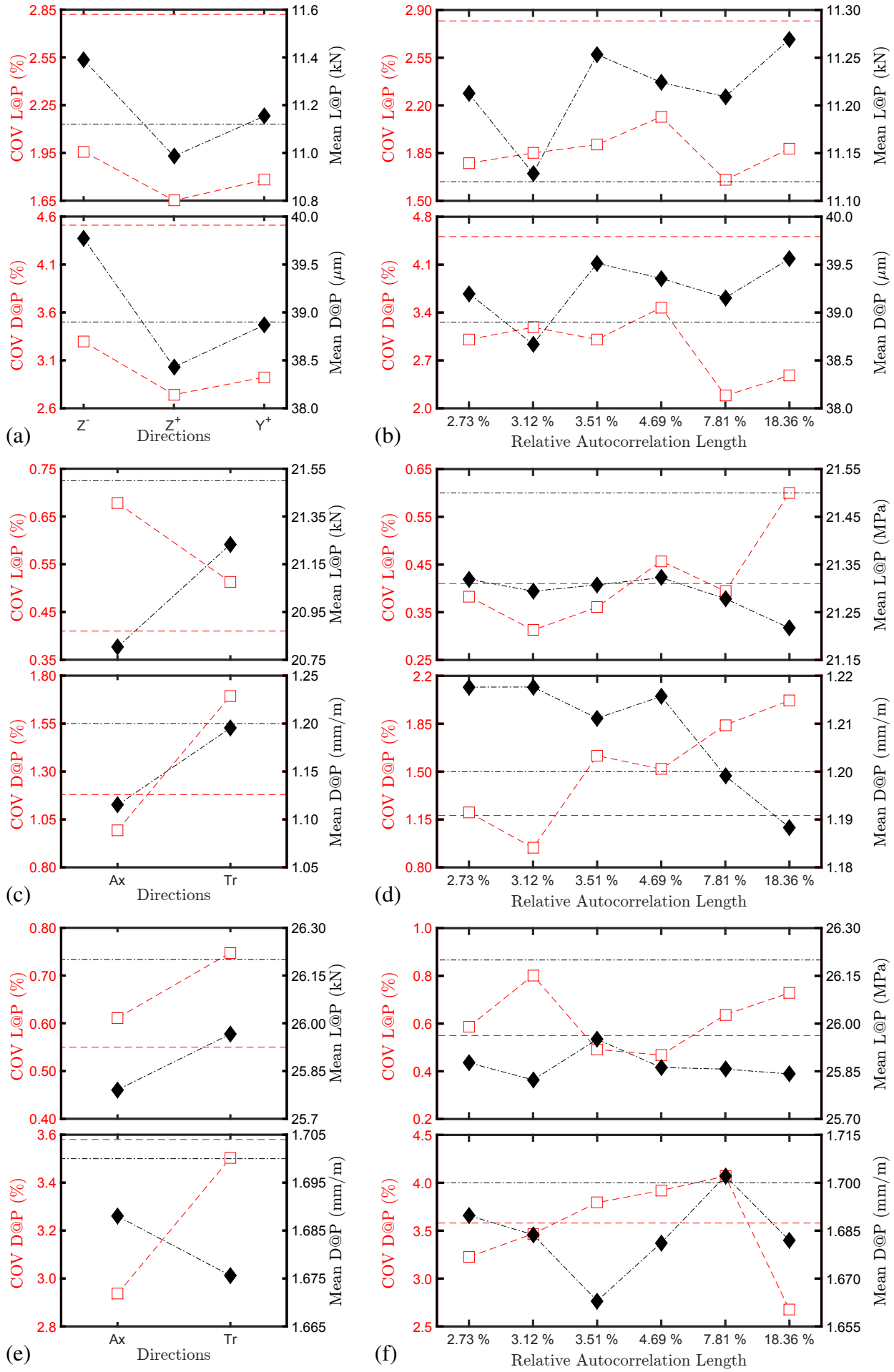

Figure 6: Normalized results for PGGF: (a-b) Beams, (c-d) cylinders, and (e-f) cubes. The straight lines represents the IRPP related results.

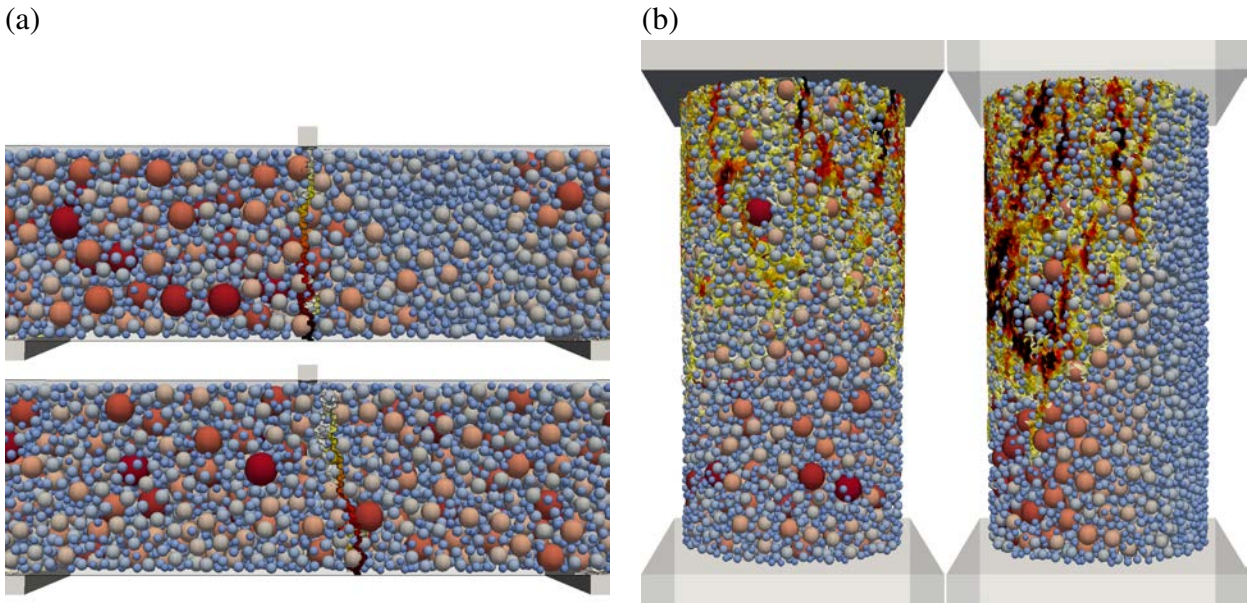

Figure 7: Different failure mechanisms for two repetitions of PGGF-R for a) beams and b) cylinders.

of any variability in the material property fields. The influence on the $L@P$ and the $D@P$ is limited in comparison with the experimental scatter. On the other hand the failure mechanisms are influenced, especially in the case of cylinders with different directional fields (see Figure 7).

5.1 Sample size

A subsampling-based analysis has been performed to evaluate the uncertainty in estimates of mean value and standard deviation with respect to sample size. For the analysis, a set of 40 simulations were run on cylinders having particles placed according to a gradient field perpendicular to the loading direction. Their result is assumed to be an independent and identically distributed sequence. From this sequence, subsamples with sizes from 2 to 38 have been randomly and non-repetitively drawn 700 times in order to ensure non-repetitiveness in boundary subsets containing exactly 2 or 38 elements, where only 780 combinations exist. The mean values and standard deviations of each subsample were calculated. Figure 8a shows the confidence bound on the mean value, while Figure 8b illustrates the uncertainty in the standard deviation. In Figure 8a, the solid line is the mean value of the original sequence. The circles are the 5% fractile of the 700 samples mean values and converge to the mean. The t-Student test was performed on each of the subsamples, in order to obtain the subsamples mean value with a 95% confidence interval. Maximum and mean values of the confidence intervals higher bound, and minimum and mean values of the confidence intervals lower bound, were recorded. The diamonds show mean higher and mean lower bounds of the confidence intervals for all the sample sizes. The squares show maximum higher and minimum lower bounds of the confidence intervals for all the sample sizes. From the results, 5 realizations of LDPM simulations appear to be a reasonable compromise in order to obtain a good approximation of the real mean value while limiting the computational cost.

A similar analysis was performed for the standard deviation as shown in Figure 8b. The estimation of the standard deviation confidence intervals is based on the χ-square test. It becomes clear that the confidence bounds converge much slower. Thus, approximately 15-20 realizations of LDPM simulations appear to be a reasonable compromise in order to obtain a good

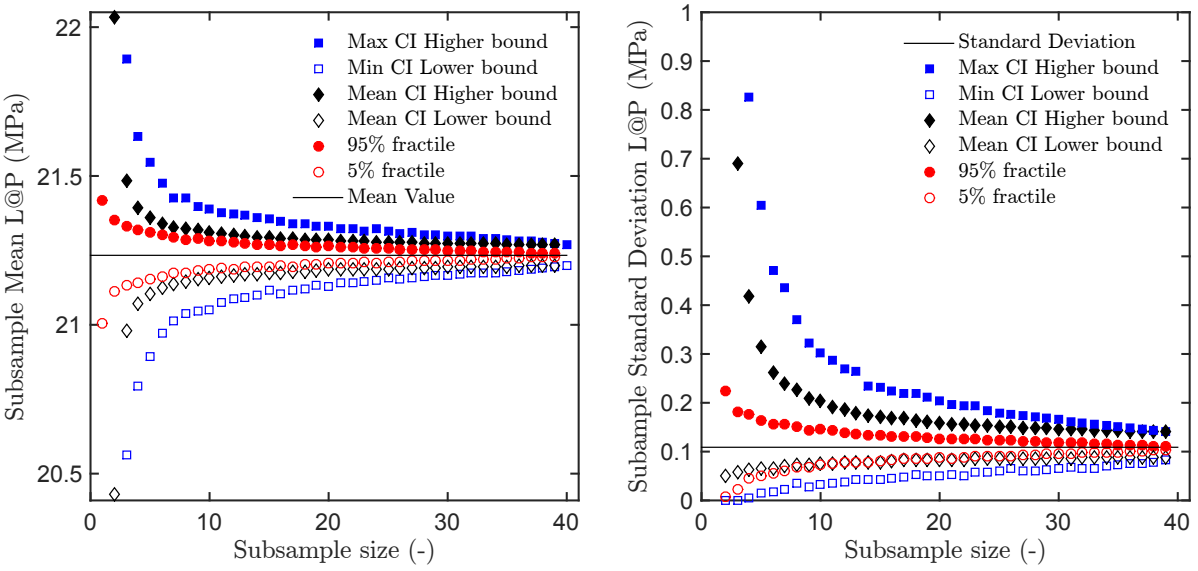

Figure 8: Subsampling-based analysis performed in order to evaluate the uncertainty of mean value and standard deviation predictions.

approximation of the real standard deviation.

6 Influence on failure mechanisms

In order to verify the observed effect of particle clustering on the failure mechanism, the three point bending tests (Figure 7a) are analyzed in detail. The compression simulations (as can be seen in Figure 7b) also show an indication of differences in the failure mechanism. The failure of the beams, on the other hand, shows a unique main crack, the end position of which can be measured and compared. The PGGF-G results are not analyzed because the three directions are symmetric along the main crack path. The results of this analysis are the crack initiation points for different autocorrelation lengths (Figure 9a) and the mean distances between the initiation points and the midspan of the beam (Figure 9b). It can be seen that the scatter in the crack initiation points is basically identical in all the cases.

Figure 9b shows a slight indication that increasing the autocorrelation length, the crack is more likely to reach larger distances from the beam center. Nevertheless, it appears that the only the placement of particles is not enough to perturbate such an output. A stronger trend was observed by Elias et al. [50], where the lattice geometry was independent and random but the material property fields were governed by random fields. From these results it can be concluded that also the material properties need to be influenced by the random field in order to reproduce realistic amounts of scatter and variability in failure modes. A stronger influence of the particle placement is visible for the case pf directional fields.

7 Conclusions

A spatial variability package for LDPM has been presented, including two new abstraction levels for the discrete framework, where particle generation are governed by an initial random field or directional filed. The presented work is a first step of a larger investigation in which modeling concepts for and different sources of spatial variability in concrete are being investigated including spatially variable material property fields.

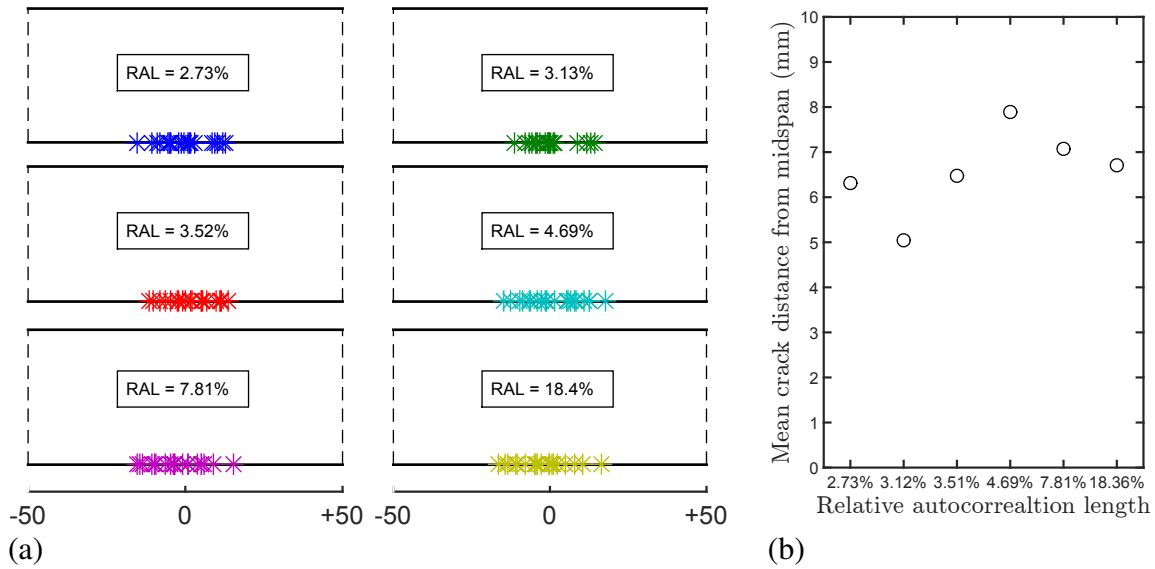

Figure 9: a) Distance between crack and beam center for different $pfse$, and b) Mean distance between crack and beams center for different autocorrelation lengths.

In order to separate the effects of particle generation process governed by random or gradient based field from randomized material property fields governed by random or gradient fields, the material property fields have been kept constant for all of the presented analyses. Thus, by considering constant material property fields, the presented results show how:

- Directional effects, mimicking production processes (concrete casting) and represented by gradient based fields, may affect the mean values of force at peak, displacement at peak, and the respective coefficients of variation;
- Correlated spatial variability models (random fields) governing the particle generation process influence the response and failure mode compared to the independent and random generation of particles;
- No clear functional dependence exists between COV of the structural response and autocorrelation length of the random field determining the particle placement and clustering, at least for the investigated geometries and chosen number of realizations.
- The investigated particle placement schemes with constant material property fields enhance the realisms of simulations but are insufficient to reproduce realistic amounts of experimental scatter.

Acknowledgments

The financial support by the Austrian Federal Ministry for Digital and Economic Affairs and the National Foundation for Research, Technology and Development is gratefully acknowledged, as well as the support of the project No. LO1408 ”AdMaS UP and FAST-S-18-5327. The computational results presented have been achieved using the Vienna Scientific Cluster (VSC).

REFERENCES

[1] R. Hill, *The mathematical theory of plasticity*, vol. 11. Oxford university press, 1998.

[2] Z. P. Bažant, "Size effect in blunt fracture: concrete, rock, metal," *Journal of Engineering Mechanics*, vol. 110, no. 4, pp. 518–535, 1984.

[3] Q. Yu, J.-L. Le, M. H. Hubler, R. Wendner, G. Cusatis, and Z. P. Bažant, "Comparison of main models for size effect on shear strength of reinforced and prestressed concrete beams," *Structural Concrete*, vol. 17, no. 5, pp. 778–789, 2016.

[4] J. Podroužek, J. Vorel, I. Boumakis, G. Cusatis, and R. Wendner, "Implications of spatial variability characterization in discrete particle models," in *Proceedings of the 9th international conference on fracture mechanics of concrete and concrete structures. Presented at the FraMCoS-9, Berkeley, CA, USA Google Scholar*, 2016.

[5] Z. P. Bazant and J.-L. Le, *Probabilistic Mechanics of Quasibrittle Structures: Strength, Lifetime, and Size Effect*. Cambridge University Press, 2017.

[6] R. E. Melchers and A. T. Beck, *Structural reliability analysis and prediction*. John Wiley & Sons, 2017.

[7] J. Podrouzek, C. Bucher, and G. Deodatis, "Identification of critical samples of stochastic processes towards feasible structural reliability applications," *Structural Safety*, vol. 47, pp. 39–47, 2014.

[8] J. Podroužek, A. Strauss, and D. Novák, "Spatial degradation in reliability assessment of ageing concrete structures," in *1st ECCOMAS thematic conference on international conference on uncertainty quantification in computational sciences and engineering. Presented at the UNCECOMP*, 2015.

[9] B. Sudret, "Probabilistic models for the extent of damage in degrading reinforced concrete structures," *Reliability Engineering & System Safety*, vol. 93, no. 3, pp. 410–422, 2008.

[10] P. Grassl and Z. P. Bažant, "Random lattice-particle simulation of statistical size effect in quasi-brittle structures failing at crack initiation," *Journal of engineering mechanics*, vol. 135, no. 2, pp. 85–92, 2009.

[11] P. Grassl and M. Jirásek, "Meso-scale approach to modelling the fracture process zone of concrete subjected to uniaxial tension," *International Journal of Solids and Structures*, vol. 47, no. 7-8, pp. 957–968, 2010.

[12] J. Podrouzek, M. Marcon, J. Vorel, and R. Wan-Wendner, "Response scatter control for discrete element models," in *Proceedings of EURO-C 2018*, 2018.

[13] J. Eliáš, M. Vořechovskỳ, J. Skoček, and Z. P. Bažant, "Stochastic discrete meso-scale simulations of concrete fracture: Comparison to experimental data," *Engineering fracture mechanics*, vol. 135, pp. 1–16, 2015.

[14] G. Cusatis, D. Pelessone, and A. Mencarelli, "Lattice discrete particle model (ldpm) for failure behavior of concrete. i: Theory," *Cement and Concrete Composites*, vol. 33, no. 9, pp. 881–890, 2011.

[15] G. Cusatis, A. Mencarelli, D. Pelessone, and J. Baylot, "Lattice discrete particle model (ldpm) for failure behavior of concrete. ii: Calibration and validation," *Cement and Concrete composites*, vol. 33, no. 9, pp. 891–905, 2011.

[16] M. Alnaggar, G. Cusatis, and G. Di Luzio, "Lattice discrete particle modeling (LDPM) of alkali silica reaction (ASR) deterioration of concrete structures," *Cement and Concrete Composites*, vol. 41, pp. 45–59, 2013.

[17] I. Boumakis, G. D. Luzio, M. Marcon, J. Vorel, and R. Wan-Wendner, "Discrete element framework for modeling tertiary creep of concrete in tension and compression," *Enginnering Fracture Mechanics (accepted)*, 2018.

[18] M. Marcon, J. Vorel, K. Ninevi, and R. Wan-Wendner, "Modeling adhesive anchors in a discrete element framework," *Materials*, vol. 10, no. 8, 2017.

[19] Q. Yu, Z. P. Bazant, and R. Wendner, "Improved algorithm for efficient and realistic creep analysis of large creep-sensitive concrete structures," *ACI Structural Journal*, vol. 109, no. 5, p. 665, 2012.

[20] Z. P. Bažant, A. B. Hauggaard, S. Baweja, and F.-J. Ulm, "Microprestress-solidification theory for concrete creep. i: Aging and drying effects," *Journal of Engineering Mechanics*, vol. 123, no. 11, pp. 1188–1194, 1997.

[21] Z. P. Bažant and S. Prasannan, "Solidification Theory for Concrete Creep. I: Formulation," *Journal of Engineering Mechanics*, vol. 115, pp. 1691–1703, 1989.

[22] I. Boumakis, M. Marcon, K. Ninevi, L.-M. Czernuschka, and R. Wan-Wendner, "Concrete creep and shrinkage effect in adhesive anchors subjected to sustained loads," *Engineering Structures*, vol. 175, pp. 790 – 805, 2018.

[23] I. Boumakis, M. Marcon, K. Ninčević, L.-M. Czernuschka, and R. Wan-Wendner, "Concrete creep effect on bond stress in adhesive fastening systems," in *Proceedings of the 3rd International Symposium on Connections between Steel and Concrete, ConSC 2017*, (Stuttgart, Germany), pp. 396–406, 2017.

[24] I. Boumakis, M. Marcon, L. Wan, and R. Wendner, "Creep and shrinkage in fastening systems," in *CONCREEP 2015: Mechanics and Physics of Creep, Shrinkage, and Durability of Concrete and Concrete Structures - Proceedings of the 10th International Conference on Mechanics and Physics of Creep, Shrinkage, and Durability of Concrete and Concrete Structures*, pp. 657–666, 2015.

[25] L. Wan, R. Wendner, B. Liang, and G. Cusatis, "Analysis of the behavior of ultra high performance concrete at early age," *Cement and Concrete Composites*, vol. 74, pp. 120–135, 2016.

[26] L. Wan-Wendner, R. Wan-Wendner, and G. Cusatis, "Age dependent size effect and fracture characteristics of ultra high performance concrete," *Cement and Concrete Composites*, vol. 84, pp. 67–82, 2018.

[27] P. B. Corson, "Correlation functions for predicting properties of heterogeneous materials. i. experimental measurement of spatial correlation functions in multiphase solids," *Journal of Applied Physics*, vol. 45, no. 7, pp. 3159–3164, 1974.

[28] B. D. Ripley, *Spatial statistics*, vol. 575. John Wiley & Sons, 2005.

[29] S. Torquato, *Random heterogeneous materials: microstructure and macroscopic properties*, vol. 16. Springer Science & Business Media, 2013.

[30] A. Tewari, A. Gokhale, J. Spowart, and D. Miracle, "Quantitative characterization of spatial clustering in three-dimensional microstructures using two-point correlation functions," *Acta Materialia*, vol. 52, no. 2, pp. 307–319, 2004.

[31] V. Lefort, G. Pijaudier-Cabot, and D. Grgoire, "Analysis by ripleys function of the correlations involved during failure in quasi-brittle materials: Experimental and numerical investigations at the mesoscale," *Engineering Fracture Mechanics*, vol. 147, pp. 449 – 467, 2015.

[32] H. Bay, A. Ess, T. Tuytelaars, and L. Van Gool, "Speeded-up robust features (surf)," *Computer vision and image understanding*, vol. 110, no. 3, pp. 346–359, 2008.

[33] N. Otsu, "A threshold selection method from gray-level histograms," *IEEE transactions on systems, man, and cybernetics*, vol. 9, no. 1, pp. 62–66, 1979.

[34] G. Christakos, *Random field models in earth sciences*. Courier Corporation, 2012.

[35] C. Schwab and R. A. Todor, "Karhunen–loève approximation of random fields by generalized fast multipole methods," *Journal of Computational Physics*, vol. 217, no. 1, pp. 100–122, 2006.

[36] S. Sakamoto and R. Ghanem, "Polynomial chaos decomposition for the simulation of non-gaussian nonstationary stochastic processes," *Journal of engineering mechanics*, vol. 128, no. 2, pp. 190–201, 2002.

[37] E. Hernández Zubeldia, L. C. de SM Ozelim, A. Luís Brasil Cavalcante, and S. Crestana, "Cellular automata and x-ray microcomputed tomography images for generating artificial porous media," *International Journal of Geomechanics*, vol. 16, no. 2, p. 04015057, 2015.

[38] C. Kloss and C. Goniva, "Liggghts–open source discrete element simulations of granular materials based on lammps," *Supplemental Proceedings: Materials Fabrication, Properties, Characterization, and Modeling*, vol. 2, pp. 781–788, 2011.

[39] J. G. Teigen, D. M. Frangopol, S. Sture, and C. A. Felippa, "Probabilistic fem for nonlinear concrete structures. i: Theory," *Journal of Structural Engineering*, vol. 117, no. 9, pp. 2674–2689, 1991.

[40] E. Syroka-Korol, J. Tejchman, and Z. Mróz, "Fe investigations of the effect of fluctuating local tensile strength on coupled energetic–statistical size effect in concrete beams," *Engineering Structures*, vol. 103, pp. 239–259, 2015.

[41] B. L. Karihaloo, "A new approach to the design of rc structures based on concrete mix characteristic length," *International Journal of Fracture*, vol. 191, no. 1-2, pp. 147–165, 2015.

[42] M. Marcon, J. Podrouzek, J. Vorel, and R. Wan-Wendner, "Characterisation of spatial variability in lattice models," in *COMUS17 - Eccomas Thematic Conference - COMPUTATIONAL MODELLING OF MULTI-UNCERTAINTY AND MULTI-SCALE PROBLEMS , ECCOMAS*, 2017.

[43] J. Podrouzek, J. Vorel, and R. Wan-Wendner, "Discrete particle placement schemes for LDPM," in *2017 EMI International Conference*, 2017.

[44] M. Vořechovskỳ and D. Novák, "-efficient random fields simulation for stochastic fem analyses," in *Computational Fluid and Solid Mechanics 2003*, pp. 2383–2386, Elsevier, 2003.

[45] J. Podroužek, J. Vorel, G. Cusatis, and R. Wendner, "Imposed correlation between random field and discrete particle placement," in *14th International Probabilistic Workshop*, pp. 245–252, Springer, 2017.

[46] D. Pelessone, "MARS: Modeling and analysis of the response of structuresUsers manual," *ES3, Beach (CA), USA*, 2009.

[47] G. Cusatis, Z. P. Bažant, and L. Cedolin, "Confinement-shear lattice model for concrete damage in tension and compression: I. theory," *Journal of Engineering Mechanics*, vol. 129, no. 12, pp. 1439–1448, 2003.

[48] R. A. Vonk, "Softening of concrete loading in compression," *Technische Universiteit Eindhoven*, 1992.

[49] S. Prabhu, S. Atamturktur, and S. Cogan, "Model assessment in scientific computing: Considering robustness to uncertainty in input parameters," *Engineering Computations*, vol. 34, no. 5, pp. 1700–1723, 2017.

[50] J. Eliáš, M. Vořechovskỳ, and J.-L. Le, "Lattice modeling of concrete fracture including material spatial randomness," *Eng Mech*, vol. 20, pp. 413–426, 2013.